iScience

CellPress
OPEN ACCESS

Article

Efficient catalytic combustion of toluene at low temperature by tailoring surficial Pt^0 and interfacial $Pt\text{-}Al(OH)_x$ species

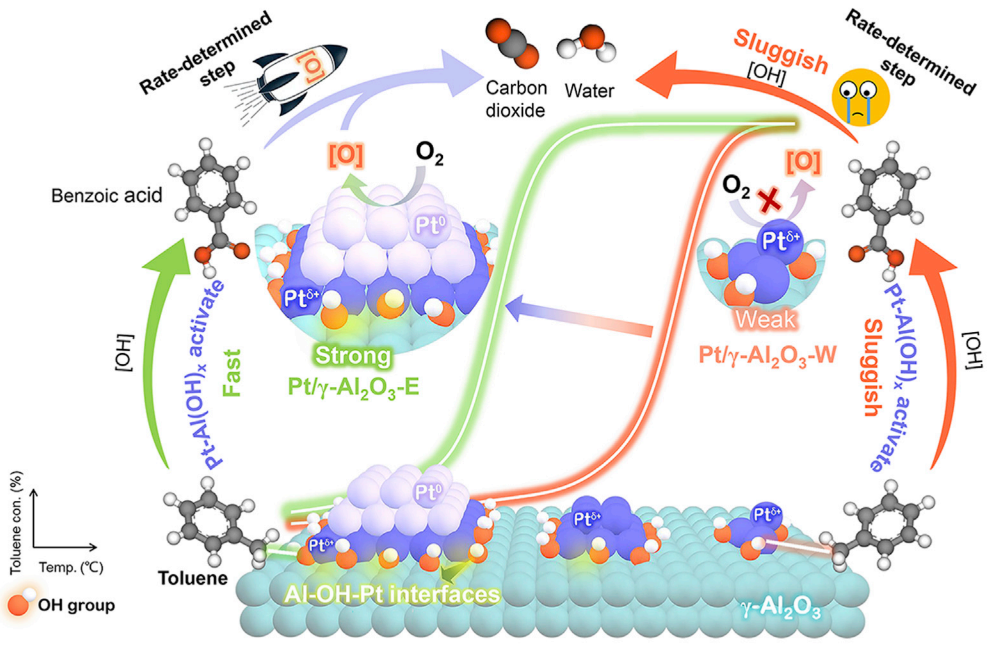

Kun Yu, Jiang Deng, Yongjie Shen, Aiyong Wang, Liyi Shi, Dengsong Zhang

dszhang@shu.edu.cn

Highlights

Efficient catalytic combustion of toluene was realized at low temperature

The excellent water resistance was achieved over Pt-based catalyst

Roles of surficial Pt^0 and interfacial $Pt\text{-}Al(OH)_x$ species were identified

In situ DRIFTS analysis revealed the reaction pathway of toluene combustion

Yu et al., iScience *24*, 102689
June 25, 2021 © 2021 The Author(s).
https://doi.org/10.1016/j.isci.2021.102689

iScience

CellPress
OPEN ACCESS

Article

Efficient catalytic combustion of toluene at low temperature by tailoring surficial Pt^0 and interfacial Pt-$Al(OH)_x$ species

Kun Yu,[1,2] Jiang Deng,[1,2] Yongjie Shen,[1] Aiyong Wang,[1] Liyi Shi,[1] and Dengsong Zhang[1,3,*]

SUMMARY

Exploring highly efficient and low-cost supported Pt catalysts is attractive for the application of volatile organic compounds (VOCs) combustion. Herein, efficient catalytic combustion of toluene at low temperature over Pt/γ-Al_2O_3 catalysts has been demonstrated by tailoring active Pt species spatially. Pt/γ-Al_2O_3 catalyst with low Pt-content (0.26 wt%) containing both interfacial Pt-$Al(OH)_x$ and surficial metallic Pt (Pt^0) species exhibited super activity and water-resistant stability for toluene oxidation. The strong metal-support interaction located at the Al-OH-Pt interfaces elongated the Pt-O bond and contributed to the oxidation of toluene. Meanwhile, the OH group at the Al-OH-Pt interfaces had the strongest adsorption and activation capability for toluene and the derived intermediate species were subsequently oxidized by oxygen species activated by surficial Pt^0 to yield carbon dioxide and water. This work initiated an inspiring sight to the design of active Pt species for the VOCs combustion.

INTRODUCTION

Volatile organic compounds (VOCs) are the crucial precursors to form secondary organic aerosol and ozone (Lewis, 2018; Shrivastava et al., 2019; Ye et al., 2018), which is deleterious to the health of human beings (Dedoussi et al., 2020; Heald and Kroll, 2020; Salthammer et al., 2018). It is urgent to develop effective elimination technologies to restrain the emissions of VOCs to reduce the atmosphere pollution (Chen et al., 2017; Wei et al., 2019). Catalytic oxidation plays an essential role in the treatment of VOCs due to its advantages of high treatment efficiency and minimal secondary pollution (Chen et al., 2020b; He et al., 2019; Hu et al., 2019). The biggest challenge is to develop highly active catalysts for the low-temperature combustion of VOCs. Supported Pt catalysts exhibit outstanding catalytic performance for VOCs combustion (Zhang et al., 2015, 2019). However, scarcity and high cost are the main concerns hindering the application of supported Pt catalysts.

Generally, the properties of supports are critical to the catalytic activity of supported Pt catalysts. Of all the supports, γ-Al_2O_3 was ranked as the most studied and used one for the catalytic combustion of VOCs, due to its large specific surface area, thermostability, and low cost (Huang et al., 2015). Besides, the particle sizes of noble metals could also regulate the chemical state of noble metals and influence their performance (Du et al., 2020; Moriau et al., 2021; Wang et al., 2020a; Zhang et al., 2020b). Several studies have proposed that the turnover frequencies (TOFs) would increase as the increase of particle size, due to the exposure of more Pt crystal facets, such as (100) and (111), which provided more active sites for the catalytic reaction (Huang et al., 2014). The strength of the surficial Pt-O bond of the Pt nanoparticles (Pt NPs) would decrease with enhanced Pt-size, and the activation energy would decrease, hence leading to higher catalytic activity (Kim and Ahn, 2009).

To further improve the performance of supported Pt catalysts, it is essential to locate the Pt active species and to understand their structure-performance relationship. Generally, Metallic Pt (Pt^0) species is considered as one of the active centers of supported Pt catalysts, which could activate O_2 even at room temperature (Duan et al., 2020; Gan et al., 2019; He et al., 2018; Liu et al., 2019b). Meanwhile, the important role of Pt^{2+} has been confirmed for the adsorption and activation of reactants for toluene oxidation (Wang et al., 2018a). Some studies implicated that the oxidized Pt (Pt–$O(OH)_x$) enabled a synergistic effect with Pt^0 and facilitated the oxidation of CO (Cao et al., 2020; Chen et al., 2020c, 2021; Cheng et al., 2019), and the OH

[1] International Joint Laboratory of Catalytic Chemistry, State Key Laboratory of Advanced Special Steel, College of Sciences, Shanghai University, Shanghai 200444, China

[2] These authors contributed equally

[3] Lead contact

*Correspondence: dszhang@shu.edu.cn

https://doi.org/10.1016/j.isci.2021.102689

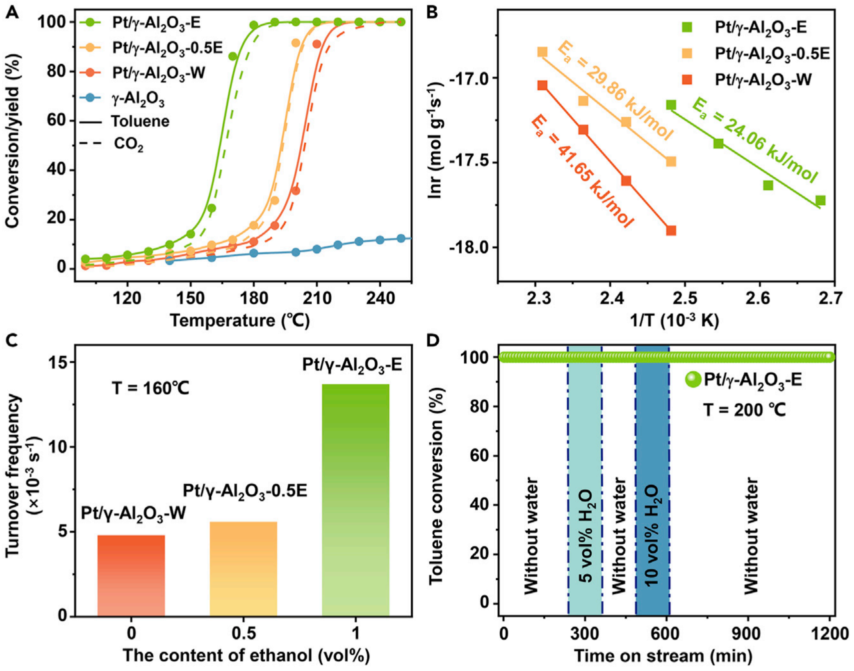

Figure 1. The catalytic performance of the Pt/γ-Al_2O_3 catalysts

(A) Plots of toluene conversion and CO_2 yield *vs.* temperature over different catalysts;

(B) Arrhenius plots;

(C) TOF_{Pt} at 160°C;

(D) Plots of thermal stability and water resistance at 200°C over Pt/γ-Al_2O_3-E. Reaction condition: 1000 ppm toluene +21% O_2/N_2 balanced, total flow rate 100 mL·min^{-1}, and WHSV = 40,000·mL g^{-1} h^{-1}.

See also Table S1.

group could facilitate the oxidation of HCHO (Wang et al., 2018b). However, the specific role of oxidized Pt species and Pt^0 for VOCs oxidation has not been clarified.

In this work, efficient catalytic combustion of toluene at low temperature over Pt/γ-Al_2O_3 catalysts has been demonstrated by tailoring active Pt species spatially. The metal-support interaction could be regulated by tuning the solvent (water or absolute ethanol) during the impregnation process giving rise to Pt particles with controlled size. More Pt^0 content on the surface of large-size Pt NPs (2.2 nm), compared with the nano Pt NPs (<1 nm), was generated during the reduction produces. Furthermore, the strong metal-support interaction located at the Al-OH-Pt interfaces in large-size Pt NPs was revealed, which contributed to high toluene adsorbed and activated ability. The degradation mechanism of toluene on the active Pt sites was revealed. Our finding initiated a novel strategy to enhance the combustion performance of VOCs at low temperature.

RESULTS

Toluene combustion performance over Pt-based catalysts

Toluene of 1000 ppm was degraded by the catalysts with weight hourly space velocity (WHSV) of 40,000 mL·g^{-1} h^{-1}. According to different ratios of ethanol to water that was used in impregnation process, the as-prepared Pt/γ-Al_2O_3 samples were labeled as Pt/γ-Al_2O_3-E (absolute ethanol), Pt/γ-Al_2O_3-0.5E (ethanol: water = 1:1) and Pt/γ-Al_2O_3-W (water). Pure γ-Al_2O_3 showed negligible catalytic activity below 250°C (Figure 1A). After loading Pt, the performance of the catalysts was dramatically improved, which confirmed Pt existed intrinsic catalytic activity for toluene combustion. The order of T_{90} (Table S1) for the three samples was as follows: Pt/γ-Al_2O_3-E (174°C) < Pt/γ-Al_2O_3-0.5E (202°C) < Pt/γ-Al_2O_3-W (212°C). The temperature of CO_2 formation showed the same tendency as toluene conversion over all three catalysts, indicating their remarkable mineralization ability. The apparent activation energy (E_a) was also calculated at toluene conversion below 20%. The E_a of Pt/γ-Al_2O_3-E calculated by the linear-fitting

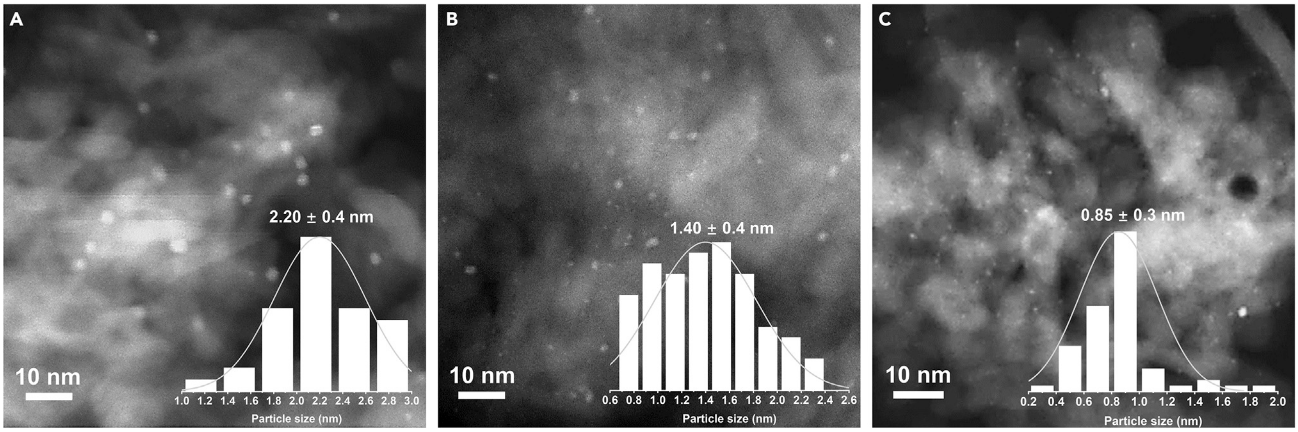

Figure 2. The distribution of Pt on the γ-Al_2O_3

HAADF-STEM images and Pt size distribution of (A) Pt/γ-Al_2O_3-E, (B) Pt/γ-Al_2O_3-0.5E, and (C) Pt/γ-Al_2O_3-W.
See also Figure S5 and Table 1.

Arrhenius equation was 24.06 kJ/mol, much lower than that of Pt/γ-Al_2O_3-W (41.65 kJ/mol) and Pt/γ-Al_2O_3-0.5E (29.86 kJ/mol) (Figure 1B), suggesting the highly efficient toluene oxidation ability of Pt/γ-Al_2O_3-E. The TOF_{Pt} was also calculated to explore the intrinsic activity of the catalysts. Pt/γ-Al_2O_3-E displayed the highest TOF_{Pt} of 13.69×10^{-3} s^{-1} at 160°C (Figure 1C and Table S1), followed by 5.59×10^{-3} s^{-1} of Pt/γ-Al_2O_3-0.5E and 4.80×10^{-3} s^{-1} of Pt/γ-Al_2O_3-W. Pt/γ-Al_2O_3-E with low Pt content had superior toluene oxidation activity in TOF_{Pt} and reaction rate compared with the state-of-the-art Pt-based catalysts (Table S2).

The thermal stability and water-resistant ability were also measured to investigate the practical application of the Pt/γ-Al_2O_3-E. Within the 20 hr of on-stream stability test at 200°C (Figure 1D), the conversion of toluene remained unchanged with 5 vol% and 10 vol% of water vapors, implying that the Pt/γ-Al_2O_3-E possessed not only outstanding catalytic activity of toluene oxidation but also tremendous catalyst stability and water-resistant ability.

Structure of Pt-based catalysts

X-ray diffraction patterns (Figure S1) suggested that the diffraction peaks of all the samples were assigned to γ-Al_2O_3 (PDF#10-0425). The absence of Pt diffraction peak suggested the excellent dispersion of Pt on the γ-Al_2O_3. The high angle annular dark-filed scanning transmission electron microscopy (HAADF-STEM) images and the energy-dispersive spectrometer line scan data (Figures S2–S4) demonstrated the existence of Pt. Figure 2 showed the Pt nanoparticle size distribution of the catalysts. The average Pt particle size of the catalysts followed the order: Pt/γ-Al_2O_3-E (2.20 ± 0.4 nm, Figure 2A) > Pt/γ-Al_2O_3-0.5E (1.40 ± 0.4 nm, Figure 2B) > Pt/γ-Al_2O_3-W (0.85 ± 0.3 nm, Figure 2C). Pt NPs on the Pt/γ-Al_2O_3-E (Figure S5A) and Pt/γ-Al_2O_3-0.5E (Figure S5B) samples had typical (111) facets. The Pt facets on the Pt/γ-Al_2O_3-W sample were hard to detect due to the small size of Pt. Other physical structure properties of the catalysts were listed in Table 1. The actual Pt loading of the Pt/γ-Al_2O_3 catalyst was close to the theoretical value. The S_{BET} (Figure S6 and Table 1) and the pore volume of the γ-Al_2O_3 almost did not change after loading Pt.

Chemical properties of Pt species

X-ray absorption fine structure (XAFS) could detect the chemical states and coordination environment of Pt species. The white line intensity of X-ray absorption near edge structure (XANES) spectra at the Pt L_3-edge of all Pt/γ-Al_2O_3 catalysts were positioned between the Pt foil and PtO_2 (Figure 3A), suggesting the presence of both metallic Pt and PtO_x in the three samples. The white line intensity of Pt/γ-Al_2O_3-E sample was closer to that of Pt foil, while the white line intensity of Pt/γ-Al_2O_3-0.5E and Pt/γ-Al_2O_3-W were nearer to the PtO_2. The results implied that more metallic Pt species existed in the Pt/γ-Al_2O_3-E, and more PtO_x existed in the Pt/γ-Al_2O_3-0.5E which was similar as Pt/γ-Al_2O_3-W (Ma et al., 2019). Extended X-ray absorption fine structure spectroscopy (EXAFS) offered more evidence about the dispersion of Pt species and the coordination environment of Pt over the catalysts (Figures 3B and S7 and Table S3). The Pt-Pt contribution was

Table 1. The structure information of the catalysts

Sample	S_{BET} (m^2/g)[a]	V_{pore} (cm^3/g)[a]	Pt loading (wt%)[b]	Pt dispersity (D_{Pt})[c]	d_{Pt} (nm)[d]
Pt/γ-Al_2O_3-E	133.3	0.60	0.260	0.669	2.20 ± 0.4
Pt/γ-Al_2O_3-0.5E	137.8	0.61	0.265	0.635	1.40 ± 0.4
Pt/γ-Al_2O_3-W	140.1	0.62	0.275	0.586	0.85 ± 0.3
γ-Al_2O_3	134.2	0.73	–	–	–

The BET surface areas (S_{BET}), pore volume (V_{pore}), Pt loading, Pt dispersity (D_{Pt}) and Pt mean particle diameters (d_{Pt}) of γ-Al_2O_3 and Pt/γ-Al_2O_3. See also Figures 2 and S6.

[a] Calculated from N_2 adsorption/desorption experiments.

[b] Determined by ICP-AES.

[c] Calculated by CO chemical adsorption data.

[d] Determined by HAADF-STEM.

observed at about 2.7 Å over Pt/γ-Al_2O_3-E (Figure 3B), indicating that most of the Pt NPs over Pt/γ-Al_2O_3-E was metallic Pt^0. Nevertheless, the Pt-Pt contribution was absent and only a Pt-O shell at about 1.7 Å was detected for Pt/γ-Al_2O_3-0.5E and Pt/γ-Al_2O_3-W samples, implying that the PtO_x on the Pt/γ-Al_2O_3-W and Pt/γ-Al_2O_3-0.5E was difficult to be reduced. A weak Pt-O shell was also observed over Pt/γ-Al_2O_3-E, which further implied the co-existence of oxidized Pt species and Pt^0. The structure fitting parameters were displayed in Table S3, the Pt–O bond distance of Pt/γ-Al_2O_3-W (2.00 Å) sample was as same as the PtO_2 foil (2.00 Å), while the Pt–O bond distance was longer for the Pt/γ-Al_2O_3-0.5E (2.11 Å) and Pt/γ-Al_2O_3-E (2.14 Å) compared with the counterpart of PtO_2. The elongation of the Pt–O bond was due to the sharing oxygen between Pt and γ-Al_2O_3, which favored the stronger interaction between oxidized Pt species and γ-Al_2O_3 (Gatla et al., 2016). The above results implied that the existence of Al-O-Pt interfaces in the Pt/γ-Al_2O_3 catalysts. Meanwhile, the elongation of the Pt–O bond also facilitated the activation of the surface oxygen (Shen et al., 2020).

To further reveal the chemical states of Pt species and the metal-support interaction between Pt and γ-Al_2O_3, H_2 temperature programmed reduction (H_2-TPR) was implemented. As shown in Figure 3C, a single reduction peak at 120°C that belonged to the reduction of surficial PtO_x to Pt^0 was observed for Pt/γ-Al_2O_3-E sample. For the Pt/γ-Al_2O_3-W and Pt/γ-Al_2O_3-0.5E samples, these peaks located at higher temperature, suggesting the stronger mental-support interaction between surficial PtO_x and Al_2O_3, making it difficult for the PtO_x to be reduced to Pt^0. The surficial PtO_x of large-size Pt NPs was easier to form Pt^0 under H_2 reduction, while the relatively stronger interaction between surficial PtO_x and γ-Al_2O_3 in sub-nano Pt NPs made it difficult to form Pt^0 species. Additionally, the peaks located around 420°C were ascribed to the reduction of Al-O-Pt interfaces that strongly interact with the surface OH groups of γ-Al_2O_3 (Bhogeswararao and Srinivas, 2015; Lee et al., 2020).

The interfacial Pt-Al$(OH)_x$ species could be detected by CO temperature programmed reduction (CO-TPR) experiments (Cao et al., 2020). As seen in Figure 3D, all the Pt catalysts possessed considerable Pt-Al$(OH)_x$ species. The temperature of the Pt-Al$(OH)_x$ peak ranked the order of Pt/γ-Al_2O_3-E (457°C) > Pt/γ-Al_2O_3-0.5E (431°C) > Pt/γ-Al_2O_3-W (371°C), indicating the strongest interaction between Pt-Al$(OH)_x$ species and γ-Al_2O_3 in Pt/γ-Al_2O_3-E, which matched the results of the EXAFS. Based on above results, surficial PtO_x on Pt/γ-Al_2O_3-E could transferred into Pt^0 easily and gave rise to more Pt^0 after reduction process while the strong interaction between interfacial Pt-Al$(OH)_x$ and γ-Al_2O_3 also existed. X-ray photoelectron spectroscopy was also employed to further confirm the existance of Al-OH. The peak at around 533.0 eV of O 1s was ascribed to the -OH species in the γ-Al_2O_3 sample, which proved the existence of Al(OH) species (Figure S8A) (Chen et al., 2014; Fang et al., 2013). It is worth noting that the ratio of -OH ($A_{-OH}/A_{-OH} + A_{-O-}$) increased after the Pt was supported (Figures S8B–S8D), indicating the coordination of Pt species with -OH, which was consisted with the CO-TPR results (Chen et al., 2021).

Oxygen adsorption and activation properties

He-temperature programmed desorption-mass spectrometry (TPD-MS) and O_2-TPD-MS were carried out to further detect the oxygen species of the catalysts. As is shown in Figure S9, the desorption of H_2O (m/z = 18) species were ascribed to the dehydroxylation on the surface of γ-Al_2O_3(Sangnier et al., 2018). Two main desorption peaks were observed over all the samples in Figure S9A. According to

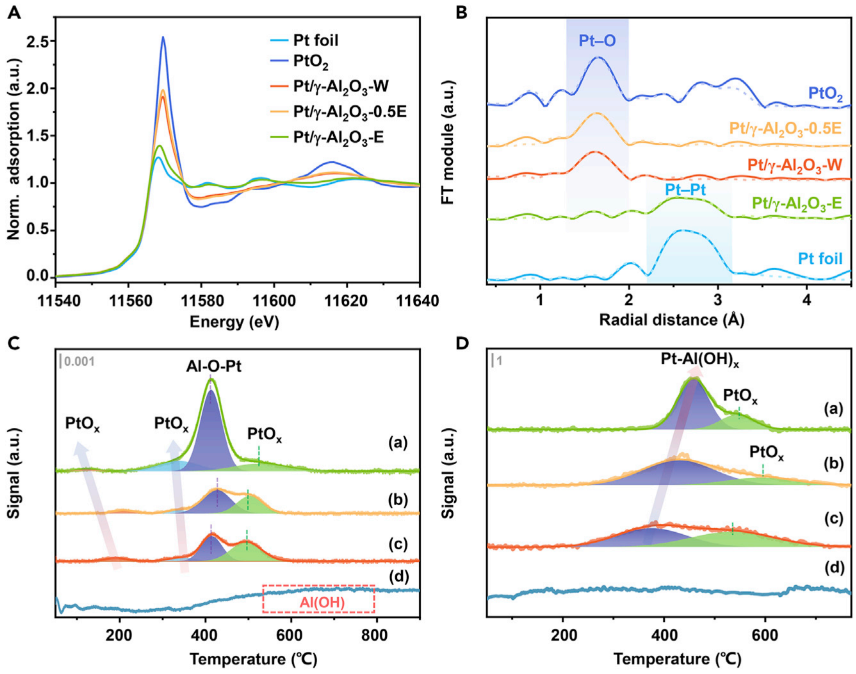

Figure 3. Chemical properties of Pt species

(A and B) (A) Normalized XANES spectra at the Pt L_3-edge of Pt foil, PtO_2 and the as-prepared catalysts, (B) magnitude of the Fourier transform (FT) k^3-weight EXAFS data for for Pt and as-prepared catalysts (dash line: fit of the experimental data), see also Figure S7 Table S3.

(C and D) (C) H_2-TPR profiles of different catalysts before H_2 reduction, (D) CO-TPR profiles of different catalysts: (a) Pt/γ-Al_2O_3-E; (b) Pt/γ-Al_2O_3-0.5E; (c) Pt/γ-Al_2O_3-W; (d) γ-Al_2O_3.

some researches, lattice OH groups were detected when the temperature beyond 400°C (Detreköy et al., 1974; Kota and Lee, 2007). Hence, the peak at low temperature (126–160°C) might come from the surface OH species, and the peak at the higher temperature (260–700°C) might be associated to the lattice OH species. The peak at low temperature shifted to higher temperature with introducing Pt (Figure S9A), which might be ascribed to the formation of Pt-Al$(OH)_x$ species. After pre-adsorption of O_2, the first peak shifted to lower temperature (<100°C). Moreover, an extra peak appeared in the temperature range of 140-259°C for all three Pt/γ-Al_2O_3 samples in the presence of oxygen, which might be attributed to the overflow of O_2 over Pt species (Figure S9B), further indicating that the loaded Pt could activate O_2. Figures 4A and 4B displayed the signal of O (m/z = 16) fragments that observed in He-TPD and O_2-TPD, respectively. In order to remove the interference of water and O_2, the signals of both had been excluded proportionally. Only Pt/γ-Al_2O_3-E sample had a desorption peak at 130°C (Figure 4A), which could be attributed to the desorption of surface adsorbed active oxygen species (O_{ad}). After pre-adsorbing O_2, the temperature of the O_{ad} peak for Pt/γ-Al_2O_3-E shifted to 88°C, which was lower than that of Pt/γ-Al_2O_3-0.5E (131°C) and Pt/γ-Al_2O_3-W (149°C) (Figure 4B). The peak intensity of O_{ad} for Pt/γ-Al_2O_3-E was the largest among all three catalysts. These profiles proved that Pt/γ-Al_2O_3-E possessed outstanding O_2 activation ability at low temperature which could facilitate the oxidation of toluene.

Toluene adsorption properties

Toluene-TPD-MS was used to measure the toluene adsorption ability of the catalysts. Figures 4C and 4D displayed the mass spectra of toluene and CO_2, respectively. The desorption temperature of toluene for the three samples was similar (~85°C), but the peak area was reduced in the order of γ-Al_2O_3 > Pt/γ-Al_2O_3-W > Pt/γ-Al_2O_3-0.5E > Pt/γ-Al_2O_3-E (Figure 4C). The existence of CO_2 indicated that toluene could be oxidized on the as-prepared Pt/γ-Al_2O_3 catalysts even without oxygen (Figure 4D). Interestingly, the order of desorption peak area of CO_2 was the reverse of that of toluene, indicating that more adsorbed toluene over Pt/γ-Al_2O_3-E was oxidized into CO_2 with increasing temperature. In order to observe the difference more intuitively, the toluene and CO_2 desorption peak area were normalized by that of γ-Al_2O_3

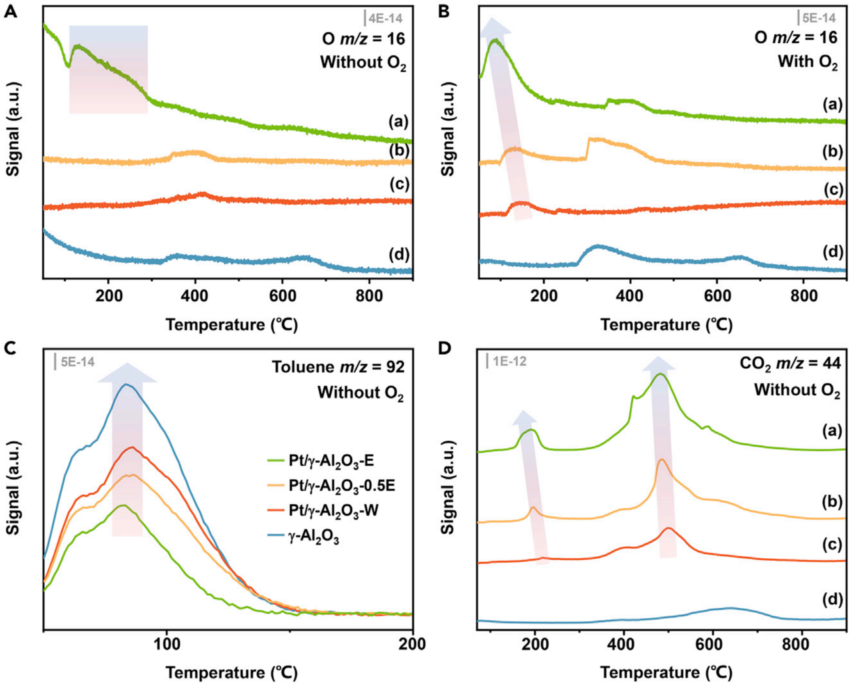

Figure 4. Reactants adsorption and activation ability over the catalysts

(A and B) (A) He-TPD-MS (*m/z* = 16, O), (B) O_2-TPD–MS (*m/z* = 16, O), (the signals of H_2O and O_2 had been excluded proportionally), see also Figure S9.

(C and D) (C) Toluene-TPD-MS (*m/z* = 92, toluene), and (D) *m/z* = 44, CO_2 profiles of different catalysts: (a) Pt/γ-Al_2O_3-E; (b) Pt/γ-Al_2O_3-0.5E; (c) Pt/γ-Al_2O_3-W; (d) γ-Al_2O_3.

See also Figure S10.

(Figure S10). With the increase of Pt size, the desorption amount of toluene decreased, while the produced CO_2 increased. According to the above results, there was more chemical adsorbed or activated toluene on the Pt/γ-Al_2O_3-E than Pt/γ-Al_2O_3-W and Pt/γ-Al_2O_3-0.5E. Furthermore, the low-temperature desorption sequence of CO_2 over the catalysts was as follows: Pt/γ-Al_2O_3-E (191°C) < Pt/γ-Al_2O_3-0.5E (197°C) < Pt/γ-Al_2O_3-W (215°C) (Figure 4D). These results indicated that Pt/γ-Al_2O_3-E had the highest low-temperature activation and oxidation ability for toluene.

The intermediates of the toluene oxidation

In situ diffuse reflectance infrared Fourier transform spectroscopy (DRIFTS) was operated to investigate the intermediate species on the surface of catalysts during the toluene oxidation. Temperature-dependent *in situ* DRIFTS displayed in Figure 5. Details of the bands related to the adsorbed species were summarized in Table S4. The bands at 2931, 2863, and 2905 cm^{-1} belonged to the stretching of C–H in methyl (–CH_3) or methylene (–CH_2) (Besselmann et al., 2000; Qu et al., 2020; Wang et al., 2015), indicating that toluene was oxidized on the catalysts surface via methyl group (Figure 5). CO (2090–2080 cm^{-1}) was also detected due to the primary oxidation of toluene (Figure 5) (Yang et al., 2020b). The efficient accumulation and oxidation of aromatic intermediate species on the Pt/γ-Al_2O_3-E made the intensity of the C–H in benzene ring band (3072, 3034, and 2996 cm^{-1}) increased from 100°C to 170°C, and decreased rapidly above 180°C (Figure 5A) (Chen et al., 2018a, 2018b; Yang et al., 2019c; Zhao et al., 2016a). As for the Pt/γ-Al_2O_3-0.5E (Figure 5B) and Pt/γ-Al_2O_3-W (Figure 5C), the intensity of the C–H in benzene ring band (3072 cm^{-1}) did not drop until 220°C and 250°C, respectively. Benzaldehyde and benzoic acid were main aromatic intermediate species observed (Figure 5). The bands associated with benzaldehyde (2450–2560, 1653, 1648, 1625, and 1370–1390 cm^{-1}) and benzoic acid (1604, 1497, 1556 and 1426 cm^{-1}) appeared at 140°C over Pt/γ-Al_2O_3-E (Figure 5A), much lower than that of Pt/γ-Al_2O_3-0.5E (180°C, Figure 5B) and Pt/γ-Al_2O_3-W (200°C, Figure 5C) (Finocchio et al., 1995; He et al., 2011; Jiang et al., 2018; Liu et al., 2018; Sun et al., 2015; Yang et al., 2019c, 2020b; Zhao et al., 2016b). The accumulation of intermediates on the three sample was quite distinct. More benzoic acid species accumulation on Pt/γ-Al_2O_3-W sample compared with Pt/γ-Al_2O_3-E sample. As the

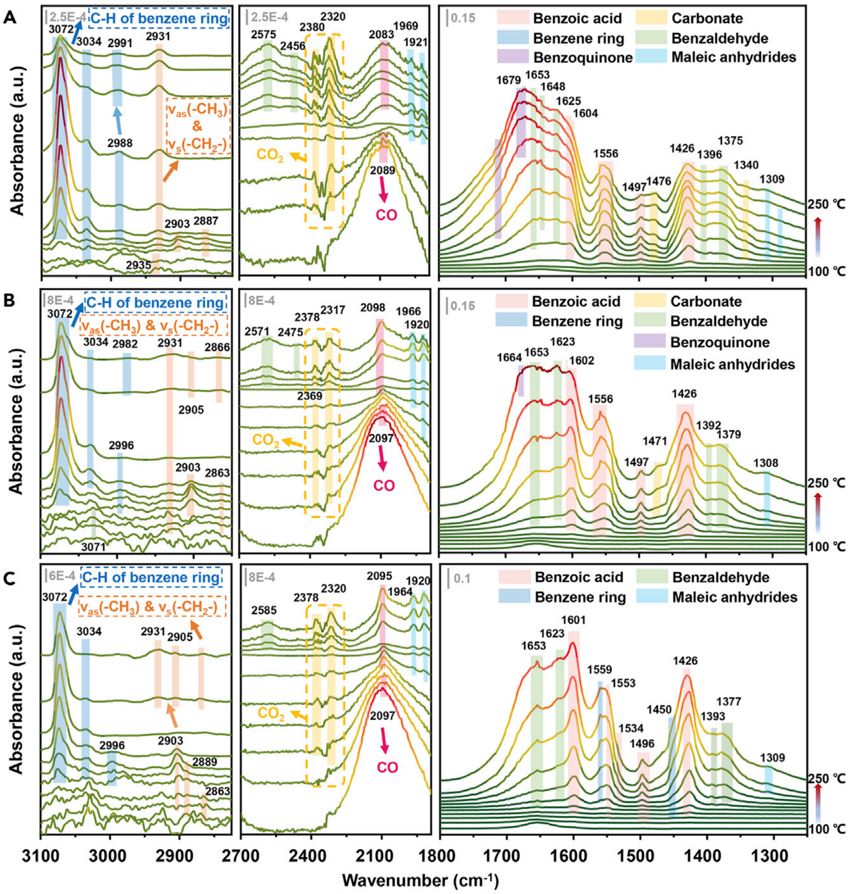

Figure 5. The main intermediates of the toluene oxidation over the as-prepared Pt/γ-Al$_2$O$_3$ catalysts

Temperature-dependent *in situ* DRIFTS spectra (3100–1350 cm^{-1}) under 500 ppm toluene + air: (A) Pt/γ-Al$_2$O$_3$-E, (B) Pt/γ-Al$_2$O$_3$-0.5E, (C) Pt/γ-Al$_2$O$_3$-W.

See also Figures S11–S13 and Table S4.

temperature rose, benzoquinone species (1715 and 1679 cm^{-1}) and maleic anhydrides (1966, 1920 and 1309 cm^{-1}) arose, because of the deeper oxidation of aromatic intermediates (Sanati and Andersson, 1993; Yang et al., 2019b, 2020a, 2020b). Benzoquinone species and maleic anhydrides presented at 190°C over Pt/γ-Al$_2$O$_3$-E (Figure 5A) but were barely detected over the Pt/γ-Al$_2$O$_3$-W until 230°C (Figure 5C), indicating the excellent low-temperature oxidation ability of Pt/γ-Al$_2$O$_3$-E. The bands at 1476 and 1340 cm^{-1} were attributed to carbonate species (Du et al., 2018; Yang et al., 2019a), and the bands ascribed to CO$_2$ appeared at around 2380 and 2320 cm^{-1} (Figure 5) (Sun et al., 2015). Other intermediate species like benzyl alcohol (3465 cm^{-1}) was also obviously observed over the Pt/γ-Al$_2$O$_3$ samples (Figure 6A) (Li et al., 2019).

Time-dependent *in situ* DRIFTS of toluene transient reaction at 190°C was operated to get the adsorption information of the toluene. All the species were detected without O$_2$ (Figures S11–S13), suggesting that the toluene could be oxidized by Pt/γ-Al$_2$O$_3$ catalysts even without oxygen, which consisted with the toluene-TPD-MS results. The vibration of C–H in benzene ring at a range from 3080 to 3000 cm^{-1} displayed different trends. The intensity of the band at 3072 cm^{-1} over Pt/γ-Al$_2$O$_3$-E (Figure S11) grew faster than that over Pt/γ-Al$_2$O$_3$-0.5E (Figure S12). Nevertheless, the intensity of this band (3072 cm^{-1}) did not increase over Pt/γ-A$_{l2}$O$_3$-W (Figure S13) until air was injected. These phenomena could be induced by various aromatic species adsorption on different catalysts. The band at 3072 cm^{-1} might be caused by the adsorption of intermediate species, and the band at 3045 and 3030 cm^{-1} over Pt/γ-Al$_2$O$_3$-W and Pt/γ-Al$_2$O$_3$-0.5E could be associated with the adsorbed toluene. It evidenced that Pt/γ-Al$_2$O$_3$-E sample possessed strong oxidation capability even without oxygen. During the adsorption of toluene, for all the catalysts, the strongest bands

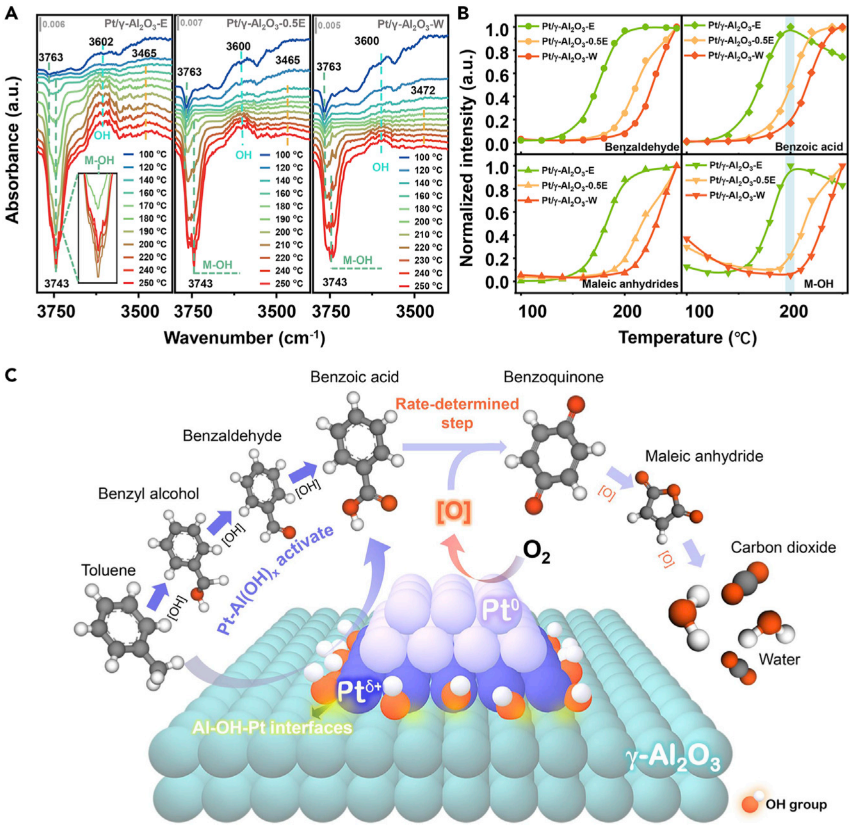

Figure 6. Proposed mechanism of toluene oxidation over Pt species

(A) Temperature-dependent *in situ* DRIFTS spectra (3800–3400 cm^{-1}) under 500 ppm toluene + air over as-prepared catalysts (left: Pt/γ-Al_2O_3-E; middle: Pt/γ-Al_2O_3-0.5E; right: Pt/γ-Al_2O_3-W), see also Figures S16–S18.

(B) Plots of normalized peak intensities at 1653 cm^{-1} (●, benzaldehyde), 1426 cm^{-1} (◆, benzoic acid), 1309 cm^{-1} (▲, maleic anhydrides) and 3743 cm^{-1} (▼, M-OH), see also Figure S19.

(C) Proposed mechanism of toluene oxidation over Pt/γ-Al_2O_3-E.

were assigned to benzoate species (1602, 1551, and 1426 cm^{-1}), indicating the accumulation of benzoic acid (Figures S11–S13). Thus, the oxidation of benzoic acid was the rate-determined step for toluene oxidation.

Gas chromatography-mass spectrometer (GC-MS) technique was adopted to get more convincing information about the intermediates during the reaction progress. As displayed in the Figure S14 and Table S5, benzyl alcohol, benzaldehyde, benzoic acid, and benzene were detected over all the three Pt/γ-Al_2O_3 catalysts at 160°C, which was consisted with the *in situ* DRIFTS results. Figure S15 exhibited the variation of the intermediates along with the temperature. The peak intensity of the toluene, benzaldehyde, and benzoic acid over Pt/γ-Al_2O_3-E sample significantly decreased when the temperature rose to 180°C. As for the Pt/γ-Al_2O_3-0.5E and Pt/γ-Al_2O_3-W samples, the peak intensity of these species did not decline until the temperature reached to 220°C. These results further demonstrated the excellent intermediates oxidation ability of the Pt/γ-Al_2O_3-E sample.

Structure-performance relationship over Pt species

Besides the intermediate species over the catalysts, the characteristic bands of hydroxyl groups presented from 3800 to 3600 cm^{-1} (Figure 6A) was associated with the OH species on the catalyst surface (Liu et al., 2018; Wang et al., 2020b). The negative band at 3763 cm^{-1} was ascribed to the presence of terminal hydroxyls, which was resulted from the adsorption and reaction between toluene and Pt-Al$(OH)_x$ (Li et al., 2020; Zhao et al., 2020). As displayed in Figure 6A, the intensity of the negative band (3763 cm^{-1}) showed a decline above 200°C for Pt/γ-Al_2O_3-E sample. However, for the other catalysts, the intensity of the negative band (3763 cm^{-1}) increased during the whole processes. A new band at 3743 cm^{-1} was observed as the temperature rose, due to the initial oxidation of toluene on the Pt-Al(OH)$_x$. The new negative band (3743 cm^{-1}) appeared at 160°C for Pt/γ-Al$_2$O$_3$-E, 200°C for Pt/γ-Al$_2$O$_3$-0.5E and 230°C for Pt/γ-Al$_2$O$_3$-W, respectively. It suggested that the lower activation temperature of toluene on the Al-OH-Pt interfaces because of the stronger metal-support interaction of Al-OH-Pt interfaces over Pt/γ-Al$_2$O$_3$-0.5E than that over Pt/γ-Al$_2$O$_3$-W. Additionally, the new band (3743 cm^{-1}) was absent during the toluene adsorbed stage at 190°C and N$_2$ purging stage but appeared over the Pt/γ-Al$_2$O$_3$-E sample after introducing air (21% O$_2$/N$_2$) at 190°C (Figure S16), indicating that the presence of O$_2$ was crucial for the further toluene oxidation at low temperature. Furthermore, there was a negative band at 3727 cm^{-1} over Pt/γ-Al$_2$O$_3$-E sample (Figure S16) during the adsorption of toluene, which also amplified the initial oxidation of toluene on the Pt-Al(OH)$_x$ sites without O$_2$. However, for the Pt/γ-Al$_2$O$_3$-0.5E (Figure S17) and Pt/γ-Al$_2$O$_3$-W (Figure S18) samples, the two bands (3743 and 3727 cm^{-1}) were missing during the whole time-dependent reaction process at 190°C. These results further confirmed that the Pt-Al(OH)$_x$ species in Pt/γ-Al$_2$O$_3$-E possessed the best adsorption and activation capability for toluene, and Pt^0 species was crucial for the oxygen activation capability at low temperature.

We normalized the band intensities of several main intermediate species (benzaldehyde, benzoic acid, maleic anhydrides) to directly observe the change of intermediate species. As shown in Figure S19, the adsorption of all species reached equilibrium after 20 min, and the purging of N$_2$ did not disturb the equilibrium, indicating the strong adsorption of toluene and intermediate species on the catalysts. The normalized intensity significantly raised after adding O$_2$ (21% O$_2$/N$_2$). It is worth noting that the generation rate of benzaldehyde and benzoate species over Pt/γ-Al$_2$O$_3$-E was opposite to Pt/γ-Al$_2$O$_3$-W. For Pt/γ-Al$_2$O$_3$-E, there was more benzoic acid formation and less benzaldehyde accumulation than Pt/γ-Al$_2$O$_3$-W, proving that Pt/γ-Al$_2$O$_3$-E had stronger oxidation ability to further oxidize benzaldehyde into benzoic acid. In contrast, the poor oxidation ability of Pt/γ-Al$_2$O$_3$-W prevented further oxidation of benzaldehyde and thus led to accumulation on the catalyst surface. Figure 6B showed the normalized intensity of the time-dependent *in situ* DRIFTS. All the species had similar generation rates at the light-off stage, but with light-off temperature in the order of Pt/γ-Al$_2$O$_3$-E < Pt/γ-Al$_2$O$_3$-0.5E < Pt/γ-Al$_2$O$_3$-W. The generation of benzaldehyde and benzoic acid over Pt/γ-Al$_2$O$_3$-E reached 1.0 at 220°C and 200°C respectively, and decreased as more benzaldehyde and benzoic acid were oxidized at high temperature. The formation of maleic anhydrides over Pt/γ-Al$_2$O$_3$-E quickly reached equilibrium at 200°C. However, the accumulation of maleic anhydrides was still ongoing at 250°C over Pt/γ-Al$_2$O$_3$-W and Pt/γ-Al$_2$O$_3$-0.5E. Coincidently, the rate change of the interaction between Pt-Al(OH)$_x$ and toluene, as well as the intermediate species (3743 cm^{-1}) was the same as that of benzoic acid (1426 cm^{-1}). The simultaneous change of the two bands not only demonstrated the adsorption of benzoic acid species at the Pt-Al(OH)$_x$ sites, and also indicated the further oxidation of the adsorbed benzoic acid. These results indicated that adsorption and activation of toluene happened at Pt-Al(OH)$_x$ sites, and adsorption/activation capability of toluene on the Pt-Al(OH)$_x$ sites increased with the improvement of the metal-support interaction of Al-OH-Pt interfaces. Meanwhile, the activation of O$_2$ at Pt^0 sites was crucial for the further oxidation of benzoic acids at low temperature, which was the rate-determined step of toluene oxidation over the Pt/γ-Al$_2$O$_3$.

Proposed mechanism of toluene oxidation over Pt/γ-Al$_2$O$_3$-E

Based on the above results, the probable toluene oxidation mechanism was proposed in Figure 6C. The degradation of toluene on the prepared Pt/γ-Al$_2$O$_3$ catalysts followed the Langmuir-Hinshelwood mechanism. Toluene was adsorbed and activated on the Pt-Al(OH)$_x$ species. According to the results of XAFS and CO-TPR, the chemical states of Pt over Pt/γ-Al$_2$O$_3$-0.5E and Pt/γ-Al$_2$O$_3$-W samples were similar, but the interaction between Pt-Al(OH)x and γ-Al$_2$O$_3$ in Pt/γ-Al$_2$O$_3$-0.5E was stronger. Therefore, compared with Pt/γ-Al$_2$O$_3$-W sample, the higher activity of Pt/γ-Al$_2$O$_3$-0.5E sample in the toluene combustion could come from its stronger interaction between Pt-Al(OH)$_x$ and γ-Al$_2$O$_3$. For Pt/γ-Al$_2$O$_3$-E sample (Figure 6C), the strongest metal-support interaction between Pt-Al(OH)$_x$ and γ-Al$_2$O$_3$ among the three samples contributed to its powerful adsorption capability which could attracted the methyl group of toluene at low temperature. Toluene was firstly adsorbed on the Pt-Al(OH)$_x$ species based on the *in situ* DRIFTS results. The aromatic ring could be adsorbed on noble metal catalysts through π-binding (Liu et al., 2019a; Wang et al., 2018a). Accordingly, toluene would be adsorbed via π-binding as the electron in d-orbital of the negatively charged Pt could back-donation to the π* of toluene (Lu et al., 2019). Therefore, the adsorption interaction bond between toluene and the Pt/γ-Al$_2$O$_3$ might be the π-binding. Generally, the alcohols, aldehydes, and acids species were detected during the oxidation of aromatic VOCs according to the former studies (Chen et al., 2019, 2020a; Zhang et al., 2020a). A similar oxidation process also happened on toluene over Pt/γ-Al_2O_3-E, the adsorbed toluene was oxidized into benzyl alcohol, benzaldehyde and then benzoic acid by OH group at Al-OH-Pt interfaces based on the *in situ* DRIFTS and GC-MS results. The oxidation of benzoic acid was the rate-determined step, which could be accelerated with abundant active oxygen species generated from the Pt^0. Benzoic acid was then oxidized to maleic anhydride and carbonates. Therefore, the strong activation capability of Pt-$Al(OH)_x$ for toluene and the excellent low temperature O_2 activation ability of Pt^0 in Pt/γ-Al_2O_3-E sample promoted its super low-temperature catalytic performance of toluene combustion.

DISCUSSION

In this work, we regulated the interaction between Pt active species and γ-Al_2O_3 by controlling the size of Pt particles over Pt/γ-Al_2O_3 with low-content of Pt (0.26 wt%) through a facile synthetic strategy. The Pt particle size was controlled by changing the content of ethanol during the one-step impregnate process. The efficient combustion of toluene at low temperature (T_{90} = 174°C, WHSV = 40,000 $mL \cdot g^{-1}$ h^{-1}) was achieved via regulating the surficial Pt^0 and interfacial Pt-$Al(OH)_x$ species. Additionally, the probable toluene degradation mechanism over the obtained catalysts was proposed according to the *in situ* DRIFTS and GC-MS results. Toluene was adsorbed on Pt-$Al(OH)_x$ sites and oxidized to benzyl alcohol, benzaldehyde, benzoic acid, maleic anhydride and carbonates. Active oxygen species generated from the Pt^0 activated gaseous oxygen promoted the processes and finally led to the total oxidation of toluene at low temperature. Compared with the previous methods, the strategy proposed here is surfactants-free which was more convenient and environment friendly. Furthermore, the super water-resistance of Pt/γ-Al_2O_3-E compared with other Pt-based catalyst also indicated its promising application in the industry. This work initiated an inspiring sight to the design of active species regulated by metal-support interaction for the VOCs combustion.

Limitations of the study

Currently, it is difficult for this research to reveal the precise change of the Pt species during the reaction. The *in situ* or *operando* XAFS would be required.

STAR★METHODS

Detailed methods are provided in the online version of this paper and include the following:

- KEY RESOURCES TABLE
- RESOURCE AVAILABILITY
  - Lead contact
  - Materials availability
  - Data and code availability
- METHOD DETAILS
  - Catalyst preparation
  - Characterization
  - Catalytic activity measurement

SUPPLEMENTAL INFORMATION

Supplemental information can be found online at https://doi.org/10.1016/j.isci.2021.102689.

ACKNOWLEDGMENTS

We acknowledge the support of the National Natural Science Foundation of China (21976117; 22006098) and the Shanghai Sailing Program (20YF1413300). The authors thank beamline BL14W1 (Shanghai Synchrotron Radiation Facility) for providing the beam time.

AUTHOR CONTRIBUTIONS

K.Y. and J.D. contributed equally to this work. They performed catalyst preparation and catalyst characterizations, prepared the figures, and co-wrote the manuscript. Y.S. analyzed the experimental results. A.W. reviewed the manuscript. L.S. provided the resources and supervised the projects. D.Z. provided the resources, supervised the projects, and contributed to the revision of this paper.

DECLARATION OF INTERESTS

The authors declare no competing interests.

Received: April 7, 2021
Revised: May 12, 2021
Accepted: June 2, 2021
Published: June 25, 2021

SUPPORTING CITATIONS

The following references appear in the supplemental information: Kondratowicz et al. (2020); Liu et al., 2019c; Pei et al. (2019); Wang et al. (2021); Wang et al. (2020c); Yang et al. (2016a); Yang et al. (2016b); Ye et al. (2018b); Zhang et al. (2018).

REFERENCES

Besselmann, S., Löffler, E., and Muhler, M. (2000). On the role of monomeric vanadyl species in toluene adsorption and oxidation on V_2O_5/TiO_2 catalysts: a Raman and in situ DRIFTS study. J. Mol. Catal. A Chem. *162*, 401–411.

Bhogeswararao, S., and Srinivas, D. (2015). Catalytic conversion of furfural to industrial chemicals over supported Pt and Pd catalysts. J. Catal. *327*, 65–77.

Cao, S., Zhao, Y., Lee, S., Yang, S., Liu, J., Giannakakis, G., Li, M., Ouyang, M., Wang, D., Sykes, E.C.H., and Flytzan-Stephanopoulos, M. (2020). High-loading single Pt atom sites Pt-$O(OH)_x$ catalyze the CO PROX reaction with high activity and selectivity at mild conditions. Sci. Adv. *6*, eaba3809.

Chen, G.X., Zhao, Y., Fu, G., Duchesne, P.N., Gu, L., Zheng, Y.P., Weng, X.F., Chen, M.S., Zhang, P., Pao, C.W., et al. (2014). Interfacial effects in iron-nickel hydroxide-platinum nanoparticles enhance catalytic oxidation. Science *344*, 495–499.

Chen, J., He, Z., Ji, Y., Li, G., An, T., and Choi, W. (2019). OH radicals determined photocatalytic degradation mechanisms of gaseous styrene in TiO_2 system under 254 nm versus 185 nm irradiation: combined experimental and theoretical studies. Appl. Catal. B Environ. *257*, 117912.

Chen, J., He, Z., Li, G., An, T., Shi, H., and Li, Y. (2017). Visible-light-enhanced photothermocatalytic activity of ABO_3-type perovskites for the decontamination of gaseous styrene. Appl. Catal. B Environ. *209*, 146–154.

Chen, J., Yi, J., Ji, Y., Zhao, B., Ji, Y., Li, G., and An, T. (2020a). Enhanced H-abstraction contribution for oxidation of xylenes via mineral particles: implications for particulate matter formation and human health. Environ. Res. *186*, 109568.

Chen, X., Chen, X., Cai, S., Chen, J., Xu, W., Jia, H., and Chen, J. (2018a). Catalytic combustion of toluene over mesoporous Cr_2O_3-supported platinum catalysts prepared by in situ pyrolysis of MOFs. Chem. Eng. J. *334*, 768–779.

Chen, X., Chen, X., Yu, E., Cai, S., Jia, H., Chen, J., and Liang, P. (2018b). In situ pyrolysis of Ce-MOF to prepare CeO_2 catalyst with obviously improved catalytic performance for toluene combustion. Chem. Eng. J. *344*, 469–479.

Chen, Y., Deng, J., Yang, B., Yan, T., Zhang, J., Shi, L., and Zhang, D. (2020b). Promoting toluene oxidation by engineering octahedral units via oriented insertion of Cu ions in the tetrahedral sites of MnCo spinel oxide catalysts. Chem. Commun. *56*, 6539–6542.

Chen, Y., Feng, Y., Li, L., Liu, J., Pan, X., Liu, W., Wei, F., Cui, Y., Qiao, B., Sun, X., et al. (2020c). Identification of active sites on high-performance Pt/Al_2O_3 catalyst for cryogenic CO oxidation. ACS Catal. *10*, 8815–8824.

Chen, Y., Lin, J., Li, L., Pan, X., Wang, X., and Zhang, T. (2021). Local structure of Pt species dictates remarkable performance on Pt/Al_2O_3 for preferential oxidation of CO in H_2. Appl. Catal. B Environ. *282*, 119588.

Cheng, Z., Feng, B., Chen, Z., Zheng, J., Li, J., and Zuo, S. (2019). La_2O_3 modified silica-pillared clays supported PtO_x nanocrystalline catalysts for catalytic combustion of benzene. Chem. Eng. J. *392*, 123747.

Dedoussi, I.C., Eastham, S.D., Monier, E., and Barrett, S.R.H. (2020). Premature mortality related to United States cross-state air pollution. Nature *578*, 261–265.

Detreköy, E.J., Jacobs, P.A., Kalló, D., and Uytterhoeven, J.B. (1974). The nature and catalytic activity of hydroxyl groups in clinoptilolite. J. Catal. *32*, 442–451.

Du, J., Qu, Z., Dong, C., Song, L., Qin, Y., and Huang, N. (2018). Low-temperature abatement of toluene over Mn-Ce oxides catalysts synthesized by a modified hydrothermal approach. Appl. Surf. Sci. *433*, 1025–1035.

Du, X., Huang, Y., Pan, X., Han, B., Su, Y., Jiang, Q., Li, M., Tang, H., Li, G., and Qiao, B. (2020). Size-dependent strong metal-support interaction in TiO_2 supported Au nanocatalysts. Nat. Commun. *11*, 5811.

Duan, X., Qu, Z., Dong, C., and Qin, Y. (2020). Enhancement of toluene oxidation performance over $Pt/MnO_2@Mn_3O_4$ catalyst with unique interfacial structure. Appl. Surf. Sci. *503*, 144161.

Fang, R.C., Sun, Q.Q., Zhou, P., Yang, W., Wang, P.F., and Zhang, D.W. (2013). High-performance bilayer flexible resistive random access memory based on low-temperature thermal atomic layer deposition. Nanoscale Res. Lett. *8*, 92.

Finocchio, E., Busca, G., Lorenzelli, V., and Willey, R.J. (1995). The sctivation of hydrocarbon CH bonds over transition metal oxide catalysts: a FTIR study of hydrocarbon catalytic combustion over $MgCr_2O_4$. J. Catal. *151*, 204–215.

Gan, T., Chu, X., Qi, H., Zhang, W., Zou, Y., Yan, W., and Liu, G. (2019). Pt/Al_2O_3 with ultralow Pt-loading catalyze toluene oxidation: promotional synergistic effect of Pt nanoparticles and Al_2O_3 support. Appl. Catal. B Environ. *257*, 117943.

Gatla, S., Aubert, D., Agostini, G., Mathon, O., Pascarelli, S., Lunkenbein, T., Willinger, M.G., and Kaper, H. (2016). Room-temperature CO oxidation catalyst: low-temperature metal-support interaction between platinum nanoparticles and nanosized ceria. ACS Catal. *6*, 6151–6155.

He, C., Cheng, J., Zhang, X., Douthwaite, M., Pattisson, S., and Hao, Z. (2019). Recent advances in the catalytic oxidation of volatile organic compounds: a review based on pollutant sorts and sources. Chem. Rev. *119*, 4471–4568.

He, C., Jiang, Z., Ma, M., Zhang, X., Douthwaite, M., Shi, J.W., and Hao, Z. (2018). Understanding the promotional effect of Mn_2O_3 on micro-/mesoporous hybrid silica nanocubic-supported Pt catalysts for the low-temperature destruction of methyl ethyl ketone: an experimental and theoretical study. ACS Catal. *8*, 4213–4229.

He, Y., Rui, Z., and Ji, H. (2011). In situ DRIFTS study on the catalytic oxidation of toluene over V_2O_5/TiO_2 under mild conditions. Catal. Commun. *14*, 77–81.

Heald, C.L., and Kroll, J.H. (2020). The fuel of atmospheric chemistry: toward a complete description of reactive organic carbon. Sci. Adv. *6*, eaay8967.

Hu, F., Peng, Y., Chen, J., Liu, S., Song, H., and Li, J. (2019). Low content of CoO_x supported on nanocrystalline CeO_2 for toluene combustion: the importance of interfaces between active sites and supports. Appl. Catal. B Environ. *240*, 329–336.

Huang, H., Hu, P., Huang, H., Chen, J., Ye, X., and Leung, D.Y.C. (2014). Highly dispersed and active supported Pt nanoparticles for gaseous formaldehyde oxidation: influence of particle size. Chem. Eng. J. *252*, 320–326.

Huang, H., Xu, Y., Feng, Q., and Leung, D.Y.C. (2015). Low temperature catalytic oxidation of volatile organic compounds: a review. Catal. Sci. Technol. *5*, 2649–2669.

Jiang, Z., Chen, C., Ma, M., Guo, Z., Yu, Y., and He, C. (2018). Rare-earth element doping-promoted toluene low-temperature combustion over mesostructured CuMCeO$_x$ (M = Y, Eu, Ho, and Sm) catalysts: the indispensable role of in situ generated oxygen vacancies. Catal. Sci. Technol. *8*, 5933–5942.

Kim, K.J., and Ahn, H.G. (2009). Complete oxidation of toluene over bimetallic Pt–Au catalysts supported on ZnO/Al$_2$O$_3$. Appl. Catal. B Environ. *91*, 308–318.

Kondratowicz, T., Drozdek, M., Michalik, M., Gac, W., Gajewska, M., and Kuśtrowski, P. (2020). Catalytic activity of Pt species variously dispersed on hollow ZrO$_2$ spheres in combustion of volatile organic compounds. Appl. Surf. Sci. *513*, 145788.

Kota, R., and Lee, B.I. (2007). Effect of lattice hydroxyl on the phase transition and dielectric properties of barium titanate particles. J. Mater. Sci. Mater. Electron. *18*, 1221–1227.

Lee, J., Jang, E.J., Oh, D.G., Szanyi, J., and Kwak, J.H. (2020). Morphology and size of Pt on Al$_2$O$_3$: the role of specific metal-support interactions between Pt and Al$_2$O$_3$. J. Catal. *385*, 204–212.

Lewis, A.C. (2018). The changing face of urban air pollution. Science *359*, 744–745.

Li, J., Dong, X., Zhang, G., Cui, W., Cen, W., Wu, Z., Lee, S.C., and Dong, F. (2019). Probing ring-opening pathways for efficient photocatalytic toluene decomposition. J. Mater. Chem. A *7*, 3366–3374.

Li, J., Li, K., Lei, B., Ran, M., Sun, Y., Zhang, Y., Kim, K.H., and Dong, F. (2020). High-efficiency photocatalytic decomposition of toluene over defective InOOH: promotive role of oxygen vacancies in ring opening process. Chem. Eng. J. *413*, 127389.

Liu, J., Li, Y., Ke, J., Wang, S., Wang, L., and Xiao, H. (2018). Black NiO-TiO$_2$ nanorods for solar photocatalysis: recognition of electronic structure and reaction mechanism. Appl. Catal. B Environ. *224*, 705–714.

Liu, Y., Gao, W., Zhan, J., Bao, Y., Cao, R., Zhou, H., and Liu, L. (2019a). One-pot synthesis of Ag-H$_3$PW$_{12}$O$_{40}$-LiCoO$_2$ composites for thermal oxidation of airborne benzene. Chem. Eng. J. *375*, 121956.

Liu, Y.R., Li, X., Liao, W.M., Jia, A.P., Wang, Y.J., Luo, M.F., and Lu, J.Q. (2019b). Highly active Pt/BN catalysts for propane combustion: the roles of support and reactant-induced evolution of active sites. ACS Catal. *9*, 1472–1481.

Liu, G., Tian, Y., Zhang, B., Wang, L., and Zhang, X. (2019c). Catalytic combustion of VOC on sandwich-structured Pt@ZSM-5 nanosheets prepared by controllable intercalation. J. Hazard. Mater. *367*, 568–576.

Lu, A., Sun, H., Zhang, N., Che, L., Shan, S., Luo, J., Zheng, J., Yang, L., Peng, D.L., Zhong, C.J., and Chen, B. (2019). Surface partial-charge-tuned enhancement of catalytic activity of platinum nanocatalysts for toluene oxidation. ACS Catal. *9*, 7431–7442.

Ma, Y., Chi, B., Liu, W., Cao, L., Lin, Y., Zhang, X., Ye, X., Wei, S., and Lu, J. (2019). Tailoring of the proximity of platinum single atoms on CeO$_2$ using phosphorus boosts the hydrogenation activity. ACS Catal. *9*, 8404–8412.

Moriau, L.J., Hrnjič, A., Pavlišič, A., Kamšek, A.R., Petek, U., Ruiz-Zepeda, F., Šala, M., Pavko, L., Šelih, V.S., Bele, M., et al. (2021). Resolving the nanoparticles' structure-property relationships at the atomic level: a study of Pt-based electrocatalysts. iScience *24*, 102102.

Pei, W., Liu, Y., Deng, J., Zhang, K., Hou, Z., Zhao, X., and Dai, H. (2019). Partially embedding Pt nanoparticles in the skeleton of 3DOM Mn$_2$O$_3$: an effective strategy for enhancing catalytic stability in toluene combustion. Appl. Catal. B Environ. *256*, 117814.

Qu, W., Wang, P., Gao, M., Hasegawa, J.Y., Shen, Z., Wang, Q., Li, R., and Zhang, D. (2020). Delocalization effect promoted the indoor air purification via directly unlocking the ring-opening pathway of toluene. Environ. Sci. Technol. *54*, 9693–9701.

Salthammer, T., Zhang, Y., Mo, J., Koch, H.M., and Weschler, C.J. (2018). Assessing human exposure to organic pollutants in the indoor environment. Angew. Chem. Int. Ed. *57*, 12228–12263.

Sanati, M., and Andersson, A. (1993). DRIFT study of the oxidation and the ammoxidation of toluene over a TiO$_2$(B)-supported vanadia catalyst. J. Mol. Catal. *81*, 51–62.

Sangnier, A., Matrat, M., Nicolle, A., Dujardin, C., and Chizallet, C. (2018). Multiscale approach to the dissociative adsorption of oxygen on a highly dispersed platinum supported on γ-Al$_2$O$_3$. J. Phys. Chem. C *122*, 26974–26986.

Shen, Y., Deng, J., Impeng, S., Li, S., Yan, T., Zhang, J., Shi, L., and Zhang, D. (2020). Boosting toluene combustion by engineering Co-O strength in cobalt oxide catalysts. Environ. Sci. Technol. *54*, 10342–10350.

Shrivastava, M., Andreae, M.O., Artaxo, P., Barbosa, H.M.J., Berg, L.K., Brito, J., Ching, J., Easter, R.C., Fan, J., Fast, J.D., et al. (2019). Urban pollution greatly enhances formation of natural aerosols over the amazon rainforest. Nat. Commun. *10*, 1046.

Sun, H., Liu, Z., Chen, S., and Quan, X. (2015). The role of lattice oxygen on the activity and selectivity of the OMS-2 catalyst for the total oxidation of toluene. Chem. Eng. J. *270*, 58–65.

Wang, C., Mao, S., Wang, Z., Chen, Y., Yuan, W., Ou, Y., Zhang, H., Gong, Y., Wang, Y., Mei, B., et al. (2020a). Insight into single-atom-induced unconventional size dependence over CeO$_2$-supported Pt catalysts. Chem *6*, 752–765.

Wang, F., Deng, J., Impeng, S., Shen, Y., Yan, T., Chen, G., Shi, L., and Zhang, D. (2020b). Unraveling the effects of the coordination number of Mn over α-MnO$_2$ catalysts for toluene oxidation. Chem. Eng. J. *396*, 125192.

Wang, M., Zhang, F., Zhu, X., Qi, Z., Hong, B., Ding, J., Bao, J., Sun, S., and Gao, C. (2015). DRIFTS evidence for facet-dependent adsorption of gaseous toluene on TiO$_2$ with relative photocatalytic properties. Langmuir *31*, 1730–1736.

Wang, Q., Li, Y., Serrano-Lotina, A., Han, W., Portela, R., Wang, R., Bañares, M.A., and Yeung, K.L. (2021). Operando investigation of toluene oxidation over 1D Pt@CeO$_2$ derived from Pt cluster-containing MOF. J. Am. Chem. Soc. *143*, 196–205.

Wang, Q., Yeung, K.L., and Bañares, M.A. (2018a). Operando Raman-online FTIR investigation of ceria, vanadia/ceria and gold/ceria catalysts for toluene elimination. J. Catal. *364*, 80–88.

Wang, Q., Zhang, C., Shi, L., Zeng, G., Zhang, H., Li, S., Wu, P., Zhang, Y., Fan, Y., Liu, G., et al. (2018b). Ultralow Pt catalyst for formaldehyde removal: the determinant role of support. iScience *9*, 487–501.

Wang, Z., Yang, H., Liu, R., Xie, S., Liu, Y., Dai, H., Huang, H., and Deng, J. (2020c). Probing toluene catalytic removal mechanism over supported Pt nano- and single-atom-catalyst. J. Hazard. Mater. *392*, 122258.

Wei, P., Qin, D., Chen, J., Li, Y., Wen, M., Ji, Y., Li, G., and An, T. (2019). Photocatalytic ozonation mechanism of gaseous n-hexane on MO$_x$-TiO$_2$-foam nickel composite (M = Cu, Mn, Ag): unveiling the role of $^{\cdot}$OH and $^{\cdot}$O$_2^-$. Environ. Sci. Nano *6*, 959–969.

Yang, H., Deng, J., Liu, Y., Xie, S., Wu, Z., and Dai, H. (2016a). Preparation and catalytic performance of Ag, Au, Pd or Pt nanoparticles supported on 3DOM CeO$_2$-Al$_2$O$_3$ for toluene oxidation. J. Mol. Catal. A Chem. *414*, 9–18.

Yang, H., Deng, J., Liu, Y., Xie, S., Xu, P., and Dai, H. (2016b). Pt/Co$_3$O$_4$/3DOM Al$_2$O$_3$: highly effective catalysts for toluene combustion. Chin. J. Catal. *37*, 934–946.

Yang, J., Hu, S., Fang, Y., Hoang, S., Li, L., Yang, W., Liang, Z., Wu, J., Hu, J., Xiao, W., et al. (2019a). Oxygen vacancy promoted O$_2$ activation over perovskite oxide for low-temperature CO oxidation. ACS Catal. *9*, 9751–9763.

Yang, W., Su, Z., Xu, Z., Yang, W., Peng, Y., and Li, J. (2020a). Comparative study of α-, β-, γ- and δ-MnO$_2$ on toluene oxidation: oxygen vacancies and reaction intermediates. Appl. Catal. B Environ. *260*, 118150.

Yang, X., Ma, X., Yu, X., and Ge, M. (2020b). Exploration of strong metal-support interaction in zirconia supported catalysts for toluene oxidation. Appl. Catal. B Environ. *263*, 118355.

Yang, X., Yu, X., Jing, M., Song, W., Liu, J., and Ge, M. (2019b). Defective Mn$_x$Zr$_{1-x}$O$_2$ solid solution for the catalytic oxidation of toluene: insights into the oxygen vacancy contribution. ACS Appl. Mater. Interfaces *11*, 730–739.

Yang, X., Yu, X., Lin, M., Ma, X., and Ge, M. (2019c). Enhancement effect of acid treatment on Mn$_2$O$_3$ catalyst for toluene oxidation. Catal. Today *327*, 254–261.

Ye, Q., Upshur, M.A., Robinson, E.S., Geiger, F.M., Sullivan, R.C., Thomson, R.J., and Donahue, N.M. (2018). Following particle-particle mixing in atmospheric secondary organic zerosols by using isotopically labeled terpenes. Chem *4*, 318–333.

Ye, Z., Giraudon, J.M., Nuns, N., Simon, P., De Geyter, N., Morent, R., and Lamonier, J.F. (2018). Influence of the preparation method on the activity of copper-manganese oxides for toluene total oxidation. Appl. Catal. B Environ. *223*, 154–166.

Zhang, F., Jiao, F., Pan, X., Gao, K., Xiao, J., Zhang, S., and Bao, X. (2015). Tailoring the oxidation activity of Pt nanoclusters via encapsulation. ACS Catal. *5*, 1381–1385.

Zhang, H., Sui, S., Zheng, X., Cao, R., and Zhang, P. (2019). One-pot synthesis of atomically dispersed Pt on MnO_2 for efficient catalytic decomposition of toluene at low temperatures. Appl. Catal. B Environ. *257*, 117878.

Zhang, J., Rao, C., Peng, H., Peng, C., Zhang, L., Xu, X., Liu, W., Wang, Z., Zhang, N., and Wang, X. (2018). Enhanced toluene combustion performance over Pt loaded hierarchical porous MOR zeolite. Chem. Eng. J. *334*, 10–18.

Zhang, W., Li, G., Liu, H., Chen, J., Ma, S., Wen, M., Kong, J., and An, T. (2020a). Photocatalytic degradation mechanism of gaseous styrene over Au/TiO_2@CNTs: relevance of superficial state with deactivation mechanism. Appl. Catal. B Environ. *272*, 118969.

Zhang, Y., Su, X., Li, L., Qi, H., Yang, C., Liu, W., Pan, X., Liu, X., Yang, X., Huang, Y., and Zhang, T. (2020b). Ru/TiO_2 catalysts with size-dependent metal/support interaction for tunable reactivity in Fischer-Tropsch synthesis. ACS Catal. *10*, 12967–12975.

Zhao, J., Xi, W., Tu, C., Dai, Q., and Wang, X. (2020). Catalytic oxidation of chlorinated VOCs over Ru/Ti_xSn_{1-x} catalysts. Appl. Catal. B Environ. *263*, 118237.

Zhao, S., Hu, F., and Li, J. (2016a). Hierarchical core-shell Al_2O_3@Pd-CoAlO microspheres for low-temperature toluene combustion. ACS Catal. *6*, 3433–3441.

Zhao, S., Li, K., Jiang, S., and Li, J. (2016b). Pd-Co based spinel oxides derived from Pd nanoparticles immobilized on layered double hydroxides for toluene combustion. Appl. Catal. B Environ. *181*, 236–248.

STAR★METHODS

KEY RESOURCES TABLE

REAGENT or RESOURCE	SOURCE	IDENTIFIER
Chemicals, peptides, and recombinant proteins		
γ-Al_2O_3	Titan Scientific Co., Ltd	CAS: 1344-28-1
Tetraammineplatinum (II) nitrate ([Pt(NH_3)$_4$](NO_3)$_2$)	Shanghai Aladdin Biochemical Technology Co., Ltd.	CAS: 20634-12-2
Ethanol absolute	Titan Scientific Co., Ltd	CAS: 67-17-5

RESOURCE AVAILABILITY

Lead contact

Further information and requests for resources and reagents should be directed to and will be fulfilled by the lead contact, Dengsong Zhang (dszhang@shu.edu.cn)

Materials availability

This study did not generate new unique reagents. All chemicals were obtained from commercial resources and used as received.

Data and code availability

This study did not generate any datasets or code. All relevant data are available from the corresponding author (dszhang@shu.edu.cn) upon reasonable request.

METHOD DETAILS

Catalyst preparation

All catalysts were synthesized by a simple one-step wetness impregnation method. 1 g of γ-Al_2O_3 was dispersed in 40 mL of absolute ethanol, and then 1243.8 μL of [Pt(NH_3)$_4$](NO_3)$_2$ (2.015 mg·mL^{-1}) solution was adding into the suspension with stirring at room temperature. After stirring for 6 hours, the solvent was removed through rotary evaporation at 60°C and then dried at 70°C overnight. The collected samples were calcined at 300°C with Ar flow for 2 hours, following with H_2 flow at 300°C for 2.5 hours. The resulting samples were denoted as Pt/γ-Al_2O_3-E. The synthesis of Pt/γ-Al_2O_3-0.5E and Pt/γ-Al_2O_3-W was similar to that of Pt/γ-Al_2O_3-E, except that a mixed solution (ethanol: water = 1:1) and water were used instead. The actual Pt-content was detected by inductively coupled plasma atomic emission spectroscopy (ICP-AES).

Characterization

X-ray diffraction (XRD) patterns were recorded using Bruker D8 Advance diffractometer equipped with a Cu Ka radiation source and a LynxEye XE-T linear detector at a scanning rate of 8° min^{-1}.

The Specific surface area (S_{BET}) of the catalysts were recorded on an ASAP 2460 Surface Area and Porosity 81 Analyzer (Micrometrics, USA) at 77 K and based on N_2 80 adsorption/desorption isotherms recorded calculated by N_2 80 adsorption/desorption isotherms, all catalysts were degassed under vacuum at 300°C for 12 h.

High-resolution transmission electron microscope (HRTEM) and high-angle annular dark-field scanning-transmission electron-microscopy (HAADF-STEM) images were obtained on JEM-2100F (JEOL LTD, Japan) at 200kV. all samples were suspended in the ethanol and dropped onto the molybdenum grid.

The X-ray adsorption fine structure (XAFS) spectra (Pt L_3-edge) of various supported Pt catalysts and references (Pt foil and PtO_2) were collected at Bl14W1 beamline in Shanghai Synchrotron Radiation Facility (SSRF). The data was carried out in the fluorescence mode at ambient temperature. The acquired EXAFS data were processed according to the standard procedures using the ATHENA module implemented in the IFEFFIT software packages. The k^3-weighted EXAFS spectra were obtained by subtracting the post-edge background from the overall absorption and then normalizing with respect to the edge-jump step. Subsequently, k^3-weighted χ (k) data of Pt L_3-edge were Fourier transformed to real (R) space using a hanging windows (dk = 1.0 $Å^{-1}$) to separate the EXAFS contributions from different coordination shells. To obtain the quantitative structural parameters around central atoms, least-squares curve parameter fitting was performed using the ARTEMIS module of IFEFFIT software packages.

H_2 temperature programmed reduction (H_2-TPR) was performed on AutoChem II 2950 adsorption apparatus (Micromeritics, USA) equipped with the thermal conductivity (TCD) detector. Prior to H_2-TPR experiment, 50 mg of catalyst was pretreated with He flow (30 mL·min^{-1}) at 300°C for 0.5 h., then cooled down to room temperature in the He atmosphere. Finally, the reactor temperature was raised to 900°C at a constant heating rate of 10°C·min^{-1} with 50 mL·min^{-1} of 10% H_2/Ar flow. The H_2 consumption was monitored by the TCD detector.

CO temperature programmed reduction (CO-TPR) was performed on a TP 5080 (Xianquan, Tianjin, China) chemical adsorption instrument. 50 mg of catalysts was pretreated at 250°C for 1 hour in He atmosphere (30 mL·min^{-1}) and then cooled down to 50°C. Finally, the reactor temperature was raised to 900°C at a constant heating rate of 10°C·min^{-1} with 30 mL/min flow of CO. The CO consumption was monitored by the TCD detector.

X-ray photoelectron spectroscopy (XPS) was measured on a Prevac photoelectron spectrometer equipped with a VGSCIENTA R3000 hemispherical analyzer. The binding energy of O 1s were referenced to the adventitious C 1s line at 284.8 eV and the peaks were fitted by Avantage Software.

O_2 temperature-programmed desorption-mass spectrometry (O_2-TPD-MS) was performed on AutoChem II 2920 adsorption apparatus (Micrometiris, USA) with an OMNI star magic angle spinning (MAS) spectrum. 50 mg of catalyst was pretreated under He flow (30 mL·min^{-1}) at 250°C for 1 h. After cooling down to room temperature, the sample was exposed to a flow of 2 vol% O_2/H_2 for 1h, followed by He purging (50 mL·min^{-1}) for 30 min to remove weakly adsorbed O_2. Then the sample was heated from 50 to 900°C under He flow, meanwhile, the TCD signal and the content of the out let gas were recorded.

Toluene temperature-programmed desorption-mass spectrometry (toluene-TPD–MS) was performed on a VDSorb-91i-Staion (Vodo) equipped with TCD detector and an OMNI star magic angle spinning (MAS) spectrum. 50 mg of catalyst was pretreated with N_2 flow (30 mL·min^{-1}) at 250°C for 1 h and restored to room temperature. 1000 ppm of toluene/N_2 (30 mL·min^{-1}) was injected into the system for 1h, followed by N_2 purging (30 mL·min^{-1}) for 30min to remove weakly adsorbed toluene. Then, the sample was heated form 50°C to 900°C under N_2 flow, meanwhile, the TCD signal and the content of the out let gas were recorded.

In order to remove the interference of water (H_2O, m/z = 18) and O_2 (m/z = 32) for the O species (m/z = 16), the signals of both had been excluded proportionally, following by the formula:

$$S'_O = S_O - S_{H_2O} * [P_O]_{H_2O} - S_{O_2} * [P_O]_{O_2} \qquad \text{(Equation 1)}$$

Where S_O, S_{H_2O} and S_{O_2} were the initial MS signal of O species (m/z = 16), water (H_2O, m/z = 18) and O_2 (m/z = 32), respectively. $[P_O]_{H_2O}$ and $[P_O]_{O_2}$ were the proportion of O in the H_2O and O_2 MS signal.

Toluene temperature-programmed surface reaction was performed on a VDSorb-91i-Fourier Transform Infrared Spectrometer (FTIR) and *in situ* Diffuse Reflectance Infrared Fourier Transform Spectroscopy (DRIFTS) experiments were performed on an FTIR spectrometer (Nicolet is50) equipped with a Harrick DRIFT cell and an MCT/A detector. All the *in situ* DRIFTS spectra were collected by accumulating 64 scans at a 4 cm^{-1} resolution.

For the temperature-dependent *in situ* DRIFTS, the catalyst was pretreated under N_2 flow (30 mL/min) at 250°C for 1 h, the system was cooled down to 100°C while the background was collected. The sample spectrum was collected under 500 ppm of toluene/air. In order to get more details around the light-off of the catalytic activity, the recorded temperature was slightly different for the three samples. The recorded temperature was 100, 120, 140, 160, 170, 180 190, 200, 220, 240 and 250°C for Pt/γ-Al_2O_3-E;100, 120, 140, 160, 180, 190, 200, 210, 220, 240 and 250°C for Pt/γ-Al_2O_3-0.5E; 100, 120, 140, 160, 180, 200, 210, 220, 230, 240 and 250°C for Pt/γ-Al_2O_3-W.

For the time-dependent *in situ* DRIFTS, the catalyst was pretreated under N_2 flow (30 mL/min) at 250°C for 1 h, the system was cooled down to 190°C, and the background was collected. 1000 ppm toluene (10 mL$\cdot$min^{-1}) was injected into the system for 1h, followed by N_2 purging (30 mL$\cdot$min^{-1}) for 30min to remove weakly adsorbed toluene. Then, the sample was reacted at 190°C under air (21% O_2/N_2) flow. Meanwhile, the spectrum was collected during the whole process.

Chromatography-mass spectrometry (GC-MS) was performed on a 7890B GC System and 5977B MSD (Agilent Technology, USA). The off-gas during catalyst activity measurements was collected by stainless steel conditioned tubes with Tenax-TA adsorbent (Marks International, USA) for 5 min of absorption under each temperature. Then, products were desorbed on thermal desorber UNITY-xr (Marks International, USA). After desorption, these intermediates were transported to the GC-MS system to analyze.

Catalytic activity measurement

A continuous flow fixed-bed tube microreactor (Φ = 6.0 nm) was carried out to measure the catalytic activity. To investigate the performance of catalysts, 1000 ppm toluene and air (21% O_2/N_2) with total flow of 100 mL$\cdot$min^{-1} was used to investigate the performance of catalyst. 150 mg of the catalyst with 40-60 mesh was used. The equivalent of a space velocity (WHSV) was approximately 40,000 mL$\cdot$g^{-1} h^{-1}. The concentrations of outlet toluene were monitored in real-time by gas chromatography (GC-2014C, Shimadzu, Japan) equipped with flame ionization detectors (FID) and the CO_2 concentration was monitored by an infrared online gas analyzer. In the case of water vapor injection, 5 and 10 vol% H_2O was introduced by passing the feed stream through a Series II Pump (Vodo, China), and the inlet temperature was 120°C for the water to be evaporated.

The toluene conversion ($X_{Toluene}$) was calculated by the following formula:

$$X_{Toluene} = \frac{[Toluene]_{in} \pm [Toluene]_{out}}{[Toluene]_{in}} \times 100\% \qquad \text{(Equation 2)}$$

Where $[Toluene]_{in}$ was the inlet toluene concentration, $[Toluene]_{out}$ was the outlet toluene concentration.

The reaction rate (r, mol$\cdot$g$^{-1}\cdot$s^{-1}) was calculated as follow:

$$r = \frac{X * V}{W_{cat}} \qquad \text{(Equation 3)}$$

Where W_{cat} represents the catalyst weight (g), V is the toluene gas flow rate (mol$\cdot$s^{-1}).

The activation energies are calculated for toluene conversions lower than 20%, and estimate using the following Arrhenius relationship:

$$\ln r = -\frac{E_a}{RT} + C \qquad \text{(Equation 4)}$$

The activation energy (E_a) can be obtained from the slope of the resulting linear plot of ln r versus 1/T.

The turnover frequencies (TOF_{Pt}) were calculated as follow:

$$TOF_{Pt} = X_{toluene} V_{toluene} \frac{M_{Pt}}{W_{cat} X_{Pt} D_{Pt}} \qquad \text{(Equation 5)}$$

Where $X_{toluene}$ represents the toluene conversion at a certain temperature; $V_{toluene}$ is the toluene flow rate (mol$\cdot$s^{-1}); M_{Pt} is the molar weight of Pt (195.08 g$\cdot$mol^{-1}); X_{Pt} is the Pt content of the catalyst; D_{Pt} is the dispersion of Pt, measured by CO chemical adsorption on a Micromeritics AutoChem II 2920 chemical adsorption apparatus.

The dispersion of Pt ($D_{Pt)}$ was calculated as follow:

$$D_{Pt} = \frac{V_{CO} M_{Pt} F}{C_{Pt}\ W_{Cat.}} * 100\% \qquad \text{(Equation 6)}$$

Where V_{CO} is the chemisorbed CO (mol g^{-1}); M_{Pt} is the atomic weight of the Pt (g mol^{-1}); F is the stoichiometry factor (F=1); C_{Pt} is the content of Pt; and $W_{Cat.}$ is the weight of the catalyst (g).